materials

MDPI

Article

Effect of Core–Shell Rubber Nanoparticles on the Mechanical Properties of Epoxy and Epoxy-Based CFRP

Tatjana Glaskova-Kuzmina [1,*], Leons Stankevics [1], Sergejs Tarasovs [1], Jevgenijs Sevcenko [1], Vladimir Špaček [2], Anatolijs Sarakovskis [3], Aleksejs Zolotarjovs [3], Krishjanis Shmits [3] and Andrey Aniskevich [1]

[1] Institute for Mechanics of Materials, University of Latvia, Jelgavas 3, LV-1004 Riga, Latvia
[2] Synpo, S. K. Neumanna 1316, 530 02 Pardubice, Czech Republic
[3] Institute of Solid State Physics, Kengaraga 8, LV-1063 Riga, Latvia
* Correspondence: tatjana.glaskova-kuzmina@lu.lv

Abstract: The aim of the research was to estimate the effect of core–shell rubber (CSR) nanoparticles on the tensile properties, fracture toughness, and glass transition temperature of the epoxy and epoxy-based carbon fiber reinforced polymer (CFRP). Three additives containing CSR nanoparticles were used for the research resulting in a filler fraction of 2–6 wt.% in the epoxy resin. It was experimentally confirmed that the effect of the CSR nanoparticles on the tensile properties of the epoxy resin was notable, leading to a reduction of 10–20% in the tensile strength and elastic modulus and an increase of 60–108% in the fracture toughness for the highest filler fraction. The interlaminar fracture toughness of CFRP was maximally improved by 53% for ACE MX 960 at CSR content 4 wt.%. The glass transition temperature of the epoxy was gradually improved by 10–20 °C with the increase of CSR nanoparticles for all of the additives. A combination of rigid and soft particles could simultaneously enhance both the tensile properties and the fracture toughness, which cannot be achieved by the single-phase particles independently.

Keywords: epoxy; CFRP; core–shell rubber nanoparticles; tensile properties; fracture toughness; glass transition temperature

Citation: Glaskova-Kuzmina, T.; Stankevics, L.; Tarasovs, S.; Sevcenko, J.; Špaček, V.; Sarakovskis, A.; Zolotarjovs, A.; Shmits, K.; Aniskevich, A. Effect of Core–Shell Rubber Nanoparticles on the Mechanical Properties of Epoxy and Epoxy-Based CFRP. *Materials* **2022**, *15*, 7502. https://doi.org/10.3390/ma15217502

Academic Editor: Dippong Thomas

Received: 10 October 2022
Accepted: 22 October 2022
Published: 26 October 2022

1. Introduction

Epoxy resins having relatively high tensile strength and modulus of elasticity, a low creep, and a good stability at elevated temperatures are extensively used as matrices in composite technology for different applications [1,2]. Nevertheless, due to high crosslinking, they are characterized by a high degree of brittleness and a poor resistance to crack initiation/propagation [3].

Their toughness could be improved by adding core–shell rubber (CSR) nanoparticles that are made of a soft rubbery core and a rigid shell around it which are mainly manufactured by emulsion polymerization and then added to the polymer resins. In comparison with the phase-separating rubbers, this method allows the advantage of controlling the particle size by changing the core and shell diameters [4]. The materials that are usually used for the core are siloxane, butadiene, and acrylate polyurethane, while poly (methyl methacrylate) (PMMA) is preferred to be used as the shell materials due to it having a good compatibility with the epoxy polymers [5,6].

It was determined that the addition of CSR particles led to a significant reduction in the tensile properties of the epoxy resin (DGEBA) and almost no effect on its glass transition temperature (T_g) [3]. For the 15 wt.% content of CSR in the epoxy, the elastic modulus and tensile strength of the epoxy were diminished by 27 and 36%, respectively. However, for the same composition of CSR filler particles, the fracture energy was improved by 550%. Similar results were obtained for the epoxy that was filled with CSR particles from 0 to 38 vol.%, revealing a gradual increase in the T_g and Poisson's ratio and a significant

decrease in the tensile and compressive properties of the CSR-modified composites which were explained by rubber having a lower Young's modulus and a higher Poisson's ratio in comparison with the epoxy [7]. By using SEM of fracture surfaces and analytical models, several toughening mechanisms (shear band yielding, core-to-shell debonding and plastic void growth) were defined [3,7].

In general, the fracture toughness of epoxy was improved by adding both rigid and soft particles [8,9]. The rigid particles toughen the epoxy through crack pinning and crack deflection/bifurcation effects, while the toughening mechanisms of the soft particles are filler-debonding, and the subsequent void grows as well as the matrix shear band.

The research aimed to estimate the effect of core–shell rubber (CSR) particles on the tensile properties, fracture toughness and glass transition temperature of the epoxy and epoxy-based CFRP. The novelty of this work is in the multi-step approach for the evaluation of the toughening effects for both the epoxy and epoxy-based CFRP and considering their mechanical properties. The application of the proposed solution with improved fracture toughness both for the epoxy and epoxy-based CFRP could broaden their use in aerospace, automotive, marine and sporting goods due to them having a longer lifetime and enhanced safety features.

2. Materials and Methods

2.1. Materials

CHS-Epoxy 582 (Spolchemie, Usti nad Labem, Czech Republic) [10] was used as matrix material. It is a diglycidyl ether of bisphenol A (DGEBA) with a reactive diluent that has an epoxide equivalent weight (EEW) of 165–173 g/mol. This epoxy resin is recommended for different applications in composites, adhesives, wind energy, construction, electronics and corrosive coatings. The hardener Telalit 0420 (Spolchemie, Usti nad Labem, Czech Republic) which is a cycloaliphatic amine was mixed with epoxy resin at a ratio of 100:25 [11].

Three additives containing CSR nanoparticles which were dispersed in DGEBA with different particle sizes and core material ACE MX 125, 156 and 960 were supplied by Kaneka (Westerlo, Belgium). The information regarding core material and CSR size are given in Table 1. For all of the additives that were studied, the concentration of CSR nanoparticles in DGEBA was 25 wt.%, the shell material was PMMA, and the density was 1.1 g/cm^3 [12]. Carbon fiber fabric KC (0/90) in plane weave and of a specific surface of 160 g/m^2 was supplied by Havel Composites (Svésedlice, Czech Republic) [13] and used for the manufacturing of CFRP laminates.

Table 1. CSR types dispersed in the epoxy [12].

Additive Name	Core Material	CSR Size, nm
ACE MX-125	Styrene butadiene	100
ACE MX-156	Polybutadiene	100
ACE MX-960	Siloxane	300

2.2. Manufacturing of the Test Samples

For pure epoxy samples, the epoxy resin was manually mixed with the hardener for approx. 10 min and the mixture was further degassed by using the vacuum pump. For CSR-modified epoxy resin, a certain content of CSR nanoparticles (2, 4, and 6 wt.%) was added to the epoxy and manually mixed, degassed, and then mixed with the hardener for approx. 10 min. After degassing, all of the mixtures were poured into silicon molds. The curing and post-curing conditions were chosen based on supplier recommendations [10]: overnight at room temperature (RT), 2 h at 60 °C, 1 h at 80 °C, and 1 h at 120 °C.

The silicon molds were used for the manufacturing of the test samples to determine the tensile properties [14,15] and fracture toughness [16] of the epoxy and epoxy modified with CSR particles. Thus, five dog-bone samples and five tapered double cantilever beam (TDCB) samples were manufactured for each test and CSR particle type and each filler fraction.

Double cantilever beam (DCB) CFRP samples were produced by lay-up technology by using woven carbon fiber fabric $(0/90)_{12}$, which was cured at RT, cut into samples and post-cured as CSR-modified epoxy resin. The CSR nanoparticle fraction of 4 wt.% in the epoxy resin was used for the manufacturing of all of the CFRP plates based on the highest results of fracture toughness obtained for the modified epoxy in TDCB tests. At least five DCB samples were manufactured and tested for each CSR nanoparticle additive.

2.3. Testing Methods

2.3.1. Morphology Analysis

The morphology of the fracture surfaces for CFRP samples was examined by using a high-resolution SEM-FIB electron microscope Helios 5 UX (Thermo Scientific, Walthamm, MA, USA), which was operated at 1 kV and 25 pA with scan interlacing and integration to avoid charging.

2.3.2. Tensile Tests

For the test specimens of epoxy and epoxy that was modified with CSR nanoparticles, quasi-static tensile tests were performed by using Zwick 2.5 universal testing machine with a crosshead speed of 2 mm/min at RT. The tensile strength was defined as the maximal achieved value of stress in the specimen, and the elastic modulus was calculated from the slope of a secant line between 0.05 and 0.25% strain on a stress–strain plot. Five test samples per each CSR type and fraction were tested, and the values that are provided correspond to their arithmetic mean value.

2.3.3. Fracture Toughness Tests

A specimen with a sharp pre-crack is needed for the precise measurement of the stress intensity factor (SIF). TDCB specimens produced in the silicone molds had an initial notch with a 1 mm width and a round end, which may substantially increase the apparent fracture toughness of the material. Therefore, the initial pre-crack of 2–5 mm length was made in the specimen before testing by the sharp knife strike. Moreover, side grooves of a depth of approx. 2 mm were produced to minimize the crack deflection and to keep the crack path along the midplane of the specimens [16]. The tests were conducted on Zwick 2.5 universal testing machine at RT with a constant displacement rate of 1 mm/min. SIF was calculated using Mode I load for a crack length < 20 mm within a constant SIF region.

For the specimen without side grooves, the SIF can be evaluated as follows [16]:

$$K_{ng} = 2P_c \frac{\sqrt{m}}{b}, \quad (1)$$

where P_c is the critical load, b is the width of the specimen, and m is a geometrical parameter, which for the specimen of the considered geometry equals 0.6 mm^{-1}. For the specimen with side grooves, Equation (2) should be modified as

$$K_g = K_{ng}\left(\frac{b}{b_n}\right)^{0.56}, \quad (2)$$

where b_n is the reduced width of the specimen at the grooves' location, and the exponent value was determined from a series of 3D finite element simulations with grooves of different depths (see Appendix A).

2.3.4. Interlaminar Fracture Toughness Tests

The Mode I interlaminar fracture toughness tests of carbon 0/90 woven fabric laminates were carried out according to ASTM: D5528 [17] using specimens with dimensions of 25 × 3 × 125 mm^3. Though this standard was specified for unidirectional laminates, it has been successfully applied for laminates with different lay-up configurations [18]. According to this standard, a linear elastic behavior is assumed in the calculation of strain

energy release rate, which is reasonable when the zone of damage at the delamination front is small relative to the thickness of the DCB sample. Opening Mode I interlaminar fracture toughness, G_{IC}, was evaluated from the load–deflection curve at the point of deviation from linearity (NL). The NL calculation of G_{IC} considers that the delamination starts to grow from the insert in the interior of the specimen at this point. The tests were performed by using Zwick 2.5 testing machine with a crosshead speed of 1 mm/min at RT and Canon EOS40D to record photos every 3 s for the analysis of the crack propagation until a failure occurred. ImageJ 1.38x software [19] was used to estimate the delamination length in DCB samples. At least five DCB samples per each CSR type at 4 wt.% in the epoxy resin used for the impregnation of cross-ply CFRP laminates were tested.

The Modified Beam Theory [17] method was used for the calculation of Mode I interlaminar fracture toughness assuming the correction for the rotation at the delamination front (Δ):

$$G_I = \frac{3P\delta}{2b(a + |\Delta|)}, \tag{3}$$

where P is the load, δ is the load point displacement, a is the delamination length, and Δ is determined experimentally by generating the least squares plot of the cube root of compliance as a function of delamination length.

Moreover, for the specimens with loading blocks, two correction parameters—a parameter F accounting for the shortening of the moment arm and the tilting of the end blocks and a displacement parameter N accounting for the stiffening of the specimen by the blocks—are recommended [17]:

$$F = 1 - \frac{3}{10}\left(\frac{\delta}{a}\right)^2 - \frac{3}{2}\left(\frac{\delta t}{a^2}\right), \tag{4}$$

$$N = 1 - \left(\frac{L'}{a}\right)^3 - \frac{9}{8}\left[1 - \left(\frac{L'}{a}\right)^2\right]\left(\frac{\delta t}{a^2}\right) - \frac{9}{35}\left(\frac{\delta t}{a^2}\right)^2, \tag{5}$$

where L' and t are the geometrical parameters of the blocks.

Then, the corrected formula for interlaminar fracture toughness by using the Modified Beam Theory method takes the form:

$$G_I = \frac{3P\delta}{2b(a + |\Delta|)} \cdot \left(\frac{F}{N}\right). \tag{6}$$

2.3.5. Density Measurements

The density of the epoxy and epoxy that was modified with CSR particles was defined at RT by using hydrostatic weighing in isopropyl alcohol and Mettler Toledo XS205DU balance with a precision of ±0.05 mg. First, the density of isopropyl alcohol was determined by using a sinker of a known volume of 10 cm^3. Then, the mass of the samples was registered in the air (m_a) and the liquid of known density (m_l). The density of the samples was determined by the formula:

$$\rho = \frac{m_a}{m_a - m_l}(\rho_l - \rho_a) + \rho_a, \tag{7}$$

where ρ_l and ρ_a are the densities of the liquid (0.785 g/cm^3 for isopropyl alcohol) and air (0.0012 g/cm^3), respectively.

2.3.6. Thermal Mechanical Analysis

The glass transition temperature (Tg) of the epoxy and epoxy modified by CSR particles was estimated by conducting thermomechanical analysis (TMA) tests using TMA/SDTA841e (Mettler Toledo, Greifensee, Switzerland). The samples were heated from 30 to 150 °C at a heating rate of 3 °C/min and a force of 0.02 N, and then, they were

subsequently cooled. According to ASTM standard E1545 [20], the glass transition corresponds to the inflection in the dimensional change when plotted against the temperature upon which the material changes from a hard (brittle) state into a soft (rubbery) state. The glass transition temperature was evaluated as the extrapolated onset of the kink in the experimental TMA curve, which was displayed as a function of temperature. At least three tests were conducted for each CSR type and fraction, and the values that are provided correspond to their arithmetic mean value.

3. Results and Discussion

3.1. Morphology of the Fracture Surface

The microscopy analysis of the fracture surfaces of the pure epoxy-based CFRP shown in Figure 1a revealed smooth and glassy surfaces with straight and sharp crack paths, which are characteristic of a brittle damage property and a weak resistance to crack initiation and propagation [8]. No delamination on the interface between the carbon fibers and the epoxy resin was noticed. The fracture surfaces of all four wt.% CSR-modified compositions that are provided in Figure 1b–d proved that the dispersion of CSR nanoparticles was good, and no significant agglomeration of CSR nanoparticles was found. The diameter of the CSR nanoparticles which were evaluated using ImageJ software was slightly higher than the data that are provided in Table 1 by the manufacturer. For the additives ACE MX-125 and ACE-MX-156, the diameter was very similar, 126 ± 28 nm and 126 ± 26 nm, accordingly. In comparison with these two additives, the ACE MX-960 CSR particles were much larger and had a wide diameter scatter—440 ± 248 nm. It could be an indication that most of the CSR nanoparticles were debonded as particles' debonding and subsequent plastic void growth is considered one of the most important toughening mechanisms for CSR/epoxy composites [3,8,9,21].

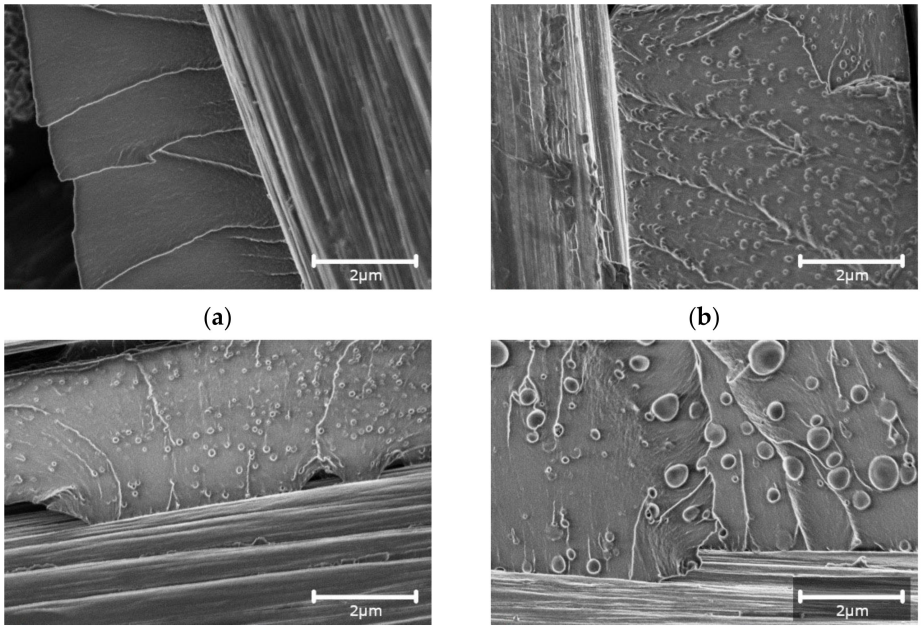

(**a**) (**b**)

(**c**) (**d**)

Figure 1. SEM images of fracture surface for the CFRP impregnated with the neat epoxy (**a**) and epoxy/CSR particles (4 wt.%) for the additives: ACE MX-125 (**b**), ACE MX-156 (**c**), and ACE MX-960 (**d**) (scale—2 µm, magnification—×25000).

For all of the CSR nanoparticle additives (Figure 1b,c), it can be noticed that the fracture surface was much rougher, and the crack paths became more curved following the CSR-particle circular shape. It could be also observed that in comparison with the

undamaged CSR nanoparticles, the ones on the crack path were not perfectly spherical, thereby revealing their valuable contribution to the crack propagation process [8].

3.2. Density and Porosity

The results that were obtained for the density of epoxy/CSR nanoparticle composites are shown in Figure 2. According to Figure 2, the addition of all of the additives containing CSR nanoparticles led to a decrease in the density of CSR-modified epoxy. By using the mixture rule, the density of the composite material could be estimated:

$$\rho_c = \rho_f \times v_f + \rho_m \times \left(1 - v_f\right), \tag{8}$$

where ρ_f and ρ_m are the density of the filler (CSR nanoparticles) and polymer matrix (epoxy), respectively, and while v_f is the volume fraction of the filler, accordingly. The density of the epoxy was experimentally found to be 1.159 ± 0.002 g/cm^3. Considering the known density of the 25%-CSR-modified epoxy of 1.1 g/cm^3 [12], the density of the CSR particles was found to be 0.91 g/cm^3 [3]. Therefore, the addition of the filler particles of a lower density to the epoxy resin has resulted in a slight decrease (by approx. 2%) of the density for the composite. The higher the filler content was, then the lower that the density of the composite was.

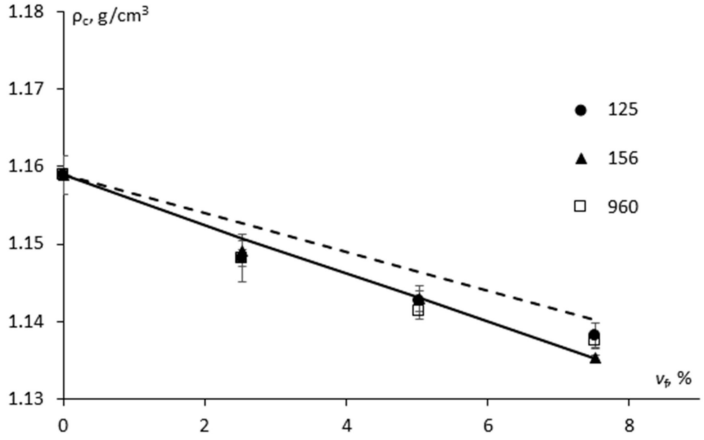

Figure 2. The density of the epoxy modified with different additives containing CSR nanoparticles (indicated on the graph) as a function of filler volume fraction (symbols—experimental data, dashed and solid lines—estimation by Equations (8) and (10), respectively.

The volume fraction of filler could be evaluated as follows [22]:

$$v_f = \frac{\rho_m \times c_f}{\rho_m \times c_f + \rho_f \times \left(1 - c_f\right)}, \tag{9}$$

where c_f is the weight fraction of the filler.

As seen in Figure 2, by using the mixture rule (Equation (8)), an overestimated value for the density of all of the CSR-modified epoxy materials was obtained. Therefore, efforts were made to evaluate the density of the composites having additional phase, air-filled pores, which could exist in the composites, and as a result, could lead to them having a lower density:

$$\rho_c = \rho_f \times v_f + \rho_p \times v_p + \rho_m \times \left(1 - v_f - v_p\right), \tag{10}$$

where ρ_p is the density of the air and v_p is the volume fraction of pores in the composites, respectively.

The volume fraction of the pores can be derived from Equation (10):

$$v_p = \frac{v_f \times \left(\rho_f - \rho_m\right) + \rho_m - \rho_c}{\rho_m - \rho_p}. \quad (11)$$

According to Figure 2, it is obvious that though the estimated volume fraction of the pores was only 0.8–2% by using the modified mixture rule (Equation (10)), a better correlation with the experimental data was obtained. It was used in the calculation of the elastic modulus of the epoxy that was filled with the CSR nanoparticles.

3.3. Tensile Properties and Glass Transition Temperature

The stress–strain curves for the epoxy and epoxy that was filled with the ACE MX-156 CSR particles are given in Figure 3a. Analogous results were obtained for the other additives. According to Figure 3b, the elastic modulus of all of the studied materials significantly decreased with the increasing CSR content. The elastic modulus of 1.99 ± 0.04 GPa was found for the unmodified epoxy. For the modified epoxy, it had the lowest value for ACE MX-960 at all of the filler fractions, which could be attributed to the lower effective stiffness of the particles due to the highest CSR size in comparison with the other additives (see Table 1) [2]. The tensile strength of the epoxy (73 ± 3 MPa) decreased by approx. 10–20% with the addition of the CSR particles. Again, slightly lower tensile strengths were found for ACE MX-960 in comparison to the other CSR nanoparticles. Moreover, it could be noted from Figure 3a that the maximal deformation increased (from 4.9 ± 0.6% to 7.2 ± 0.5%) with the increase of the CSR content, thereby revealing the plasticization/softening effect resulting from the inclusion of softer filler particles in a brittle matrix.

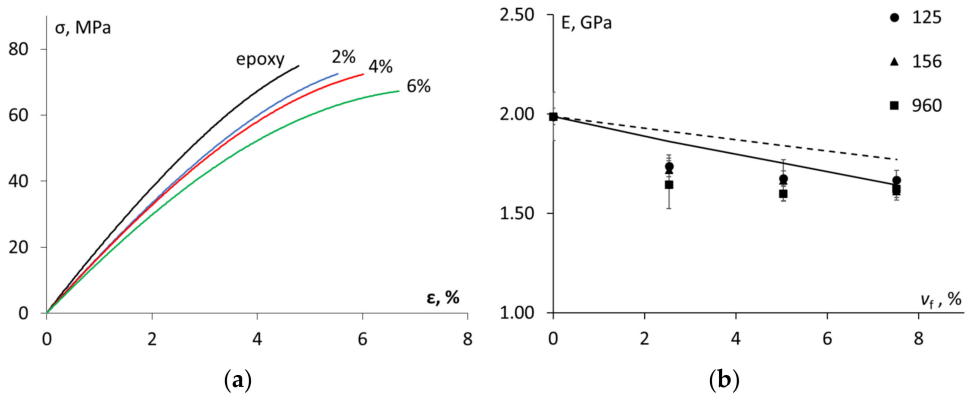

Figure 3. Stress–strain curves for the epoxy and epoxy filled with ACE MX-156 at different filler fractions indicated on the graph (**a**) and elastic modulus vs. filler volume fraction (dots -experimental results for different CSR nanoparticles, dashed and solid lines—evaluation by Equation (14) and by Equation (12), respectively (**b**).

Several analytical models, e.g., the Halpin–Tsai [3], Lewis–Nielsen [3,7] and Mori–Tanaka ones [7], were used to predict the significant reduction of the elastic modulus for the epoxy that was filled with the CSR nanoparticles. Most models epitomize an ideal composite by making several assumptions, e.g., that the polymer matrix and the filler particles are linear-elastic and isotropic, thereby having a perfect bond between them [23–25]. Moreover, the porosity and agglomeration of the filler particles negatively affecting the mechanical properties are usually neglected. In this work, the Hansen model [26,27] considering the spherical particles that are embedded in spherical shells of the matrix was used. It was applied in two steps: 1. to estimate the elastic modulus of the epoxy matrix containing a certain volume fraction of the pores from Equation (8), and 2. to determine the elastic modulus of the epoxy (with the pores) that was filled with the CSR nanoparticles.

According to the Hansen model, the elastic modulus of the matrix that was filled with spherical particles was estimated by using the following formula:

$$E_c = \frac{\left(1 - v_f\right) + \left(1 + v_f\right) E_f / E_m}{\left(1 + v_f\right) + \left(1 - v_f\right) E_f / E_m} \times E_m, \quad (12)$$

where E_f and E_m are the elastic moduli of the filler and the matrix, respectively.

For the first step considering the epoxy matrix that was filled with the pores (air bubbles), Equation (12) becomes simplified since $E_f / E_m \ll 1$, and it takes the form

$$E_c^I = \frac{(1 - v_p)}{(1 + v_p)} \times E_m. \quad (13)$$

For the second step considering the epoxy matrix (with pores) that was filled with the CSR nanoparticles, Equation (12) was modified to include both pores and CSR nanoparticles

$$E_c^{II} = \frac{\left(1 - v_f\right) + \left(1 + v_f\right) E_f / E_c^I}{\left(1 + v_f\right) + \left(1 - v_f\right) E_f / E_c^I} \times E_c^I, \quad (14)$$

where the elastic modulus of the CSR particles E_f = 4 MPa [2], and volume fraction of the filler and pores, v_f and v_p, were evaluated from Equations (9) and (11), respectively.

The results of the evaluation by Equations (12) and (14) are shown in Figure 3b. Generally, it could be concluded that at the higher filler contents, the Hansen model allowed us to predict the reduction of the elastic modulus by approx. 20% due to the addition of the soft CSR particles in the epoxy resin. It could be either noticed that the consideration of the pores (0.8–2.0 vol.%) improves the description of the experimental results. In general, the addition of ACE MX-960 to the epoxy resin led to marginally lower values of elastic modulus than those of the two other CSR-containing additives. It could indicate a higher volume of the softcore when it is compared to the total particle (core plus shell) volume since the size of these particles is the greatest when it is compared to the other ones (see Table 1).

The results that were obtained for the glass transition temperature as evaluated using the TMA diagrams are provided in Figure 4. The glass transition temperature of the epoxy was approx. 78.1 ± 2.2 °C which was within the range (70–140 °C) of the reported values of T_g for DGEBA type epoxy [3,8,28]. Contradictory results are provided in the literature revealing the occurrence of an improvement [7], a reduction [8] or almost no effect [3,4,21,28] on T_g for the epoxy with the addition of the CSR nanoparticles. According to Figure 4, a gradual increase of 10–20 °C was obtained for the epoxy that was filled with all of the additives containing the CSR nanoparticles, which could be attributed to the high crosslink density and toughening effect of rubber modifiers, thereby testifying to their dissolution in the epoxy continuous phase.

3.4. Fracture Toughness

The representative load–displacement curves for TDCB tests are provided in Figure 5a. Obviously, the soft CSR nanoparticles were effective as tougheners for the epoxy resin. According to Figure 5a, the critical load of the epoxy was significantly improved with the increase of CSR nanoparticles of ACE MX-960. Similar results were obtained for the rest of the additives containing the CSR nanoparticles.

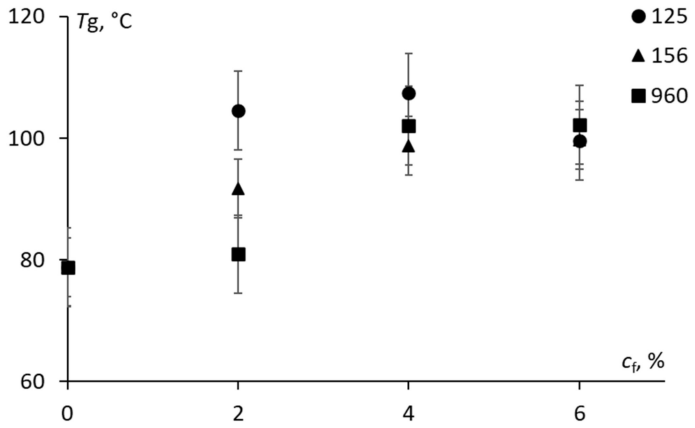

Figure 4. The glass transition temperature of the epoxy modified with different additives containing CSR nanoparticles (indicated on the graph) as a function of filler weight fraction.

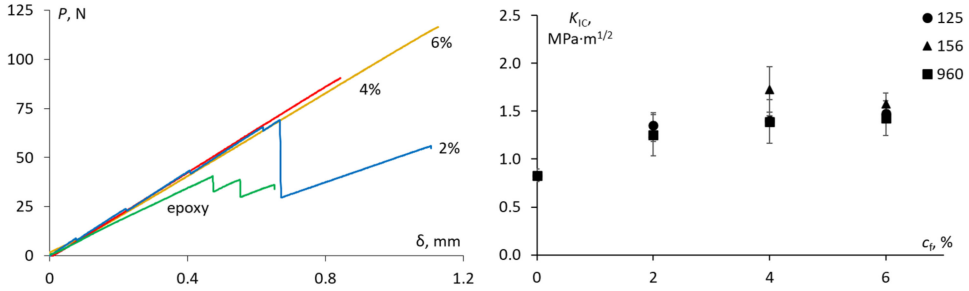

(**a**) (**b**)

Figure 5. Load–displacement curves for TDCB tests of the epoxy and epoxy filled with ACE MX-960 at different filler weight fractions indicated on the graph (**a**) and fracture toughness for the epoxy and epoxy modified with ACE MX-125, 156 and 960 at different weight filler fractions (indicated on the graph) (**b**).

The fracture toughness of the epoxy which was evaluated by Equation (2) was 0.83 ± 0.07 MPa·m$^{1/2}$ which is slightly lower than the values that are reported in the literature for the epoxy resins [7,8]. As seen in Figure 5b, the addition of the CSR nanoparticles led to a gradual improvement in the fracture toughness for all of the types of additives. No considerable distinction in the fracture toughness among the additives was detected, thereby proving that small (100 nm) and large (300 nm) CSR particles were equally efficient. Though generally, ACE MX-156 showed the greatest enhancement in the fracture toughness value which was approx. 108% at the CSR content of 4 wt.%. The optimum rubber content beyond which the fracture toughness did not improve was reported [7,28]. In this work, according to Figure 5b, the optimum CSR nanoparticle content could be estimated as 4 wt.% for all of the additives. Of course, this result is only relevant for certain dispersion conditions of the CSR particles in the epoxy. Nevertheless, the manual mixing of the CSR nanoparticles in the epoxy resulted in a good dispersion of the CSR nanoparticles as seen by the SEM and a considerable improvement in the fracture toughness. Additionally, a low fraction of pores that was indirectly estimated from the density measurements revealed the sufficient quality of the manufactured samples.

3.5. Interlaminar Fracture Toughness

The typical DCB load vs. displacement curves of the unmodified and CSR-modified CFRP laminate specimens are shown in Figure 6a. The saw-like drops on the load–displacement diagrams after the critical load was achieved were obviously caused by

the woven 0/90 lay-up configuration of the carbon fabric that was used to produce the composite laminate. According to Figure 6a, the effect of all of the additives containing the CSR nanoparticles was substantial, thereby leading to the improvement of the critical load of the CFRP by 32–70%. The Mode I interlaminar fracture toughness of CFRP which was evaluated by Equation (6) was enhanced from 390 ± 50 J/m^2 to a maximal value of 599 ± 13 J/m^2 as shown in Figure 6b for the CFRP with 4 wt.% of ACE MX-960.

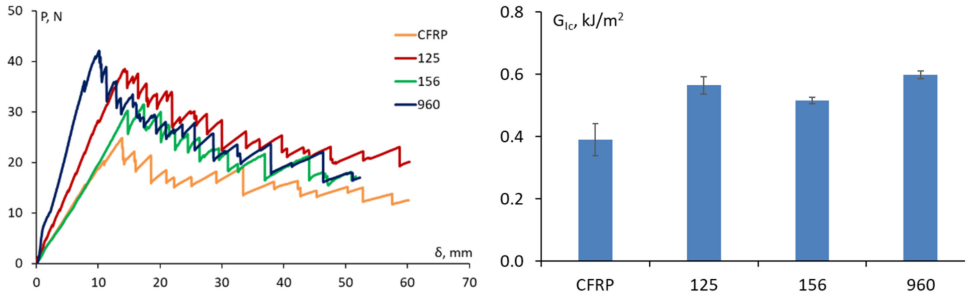

(**a**) (**b**)

Figure 6. Typical load-crack opening displacement curves for CFRP and CFRP modified with ACE MX (indicated on the graph) at 4 wt.% (**a**) and interlaminar fracture toughness evaluated by Equation (6) for different materials studied (indicated on the graph) (**b**).

However, the toughening effect of the CSR nanoparticles in the epoxy did not fully transfer to the epoxy-based CFRP composite laminates. E.g., the use of an epoxy that was modified with 4 wt.% of ACE-MX 156 having the maximal improvement of fracture toughness by 108% as a matrix for CFRP laminates resulted in the improvement to the interlaminar fracture toughness by only 32%. The interlaminar fracture toughness was maximally improved by 53% for ACE MX-960 at CSR content 4 wt.%. A further increase in the CSR fraction could result in greater improvement of the interlaminar fracture toughness of the CFRP, though, it should be emphasized that rubber toughening has also the side effect of increasing the viscosity of the epoxy resin, thereby negatively contributing to the fabrication of composite laminates [8,9,18,28]. Additionally, at higher values of the filler fraction, a significant agglomeration can occur, thereby causing a local stress concentration and a detrimental effect on the toughening performance of the filler particles [29,30].

4. Conclusions

The epoxy resin was modified by the addition of three types of CSR nanoparticles of different contents. On the one hand, the addition of all of the additives containing the soft CSR nanoparticles resulted in a minor decrease in the density, and a substantial reduction in the elastic modulus and tensile strength of the epoxy resin. The Hansen model was applied to describe the elastic modulus of the epoxy having a certain fraction of the CSR nanoparticles and pores, and a good agreement with the experimental results was found at the high CSR contents.

On the other hand, it was testified that the fracture toughness of the epoxy was significantly improved by the addition of all of the investigated types of CSR. The optimum CSR nanoparticle content was found to be 4 wt.% for all of the CSR nanoparticle types, thereby resulting in the improvement of the fracture toughness of the epoxy by 60–108%. No considerable distinction in the fracture toughness among the additives was detected, thereby proving that the small (100 nm) and large (300 nm) CSR nanoparticles were equally efficient.

Moreover, the effect of all of the additives containing the CSR nanoparticles was substantial, leading to the improvement in the interlaminar fracture toughness of the CFRP by 32–53%. Although, the toughening effect of the CSR nanoparticles in the epoxy was two times higher than it was in the epoxy-based CFRP composite laminates.

Additionally, a gradual increase of the glass transition temperature was obtained for the epoxy that was filled with all of the additives containing CSR nanoparticles, which

could be attributed to the high crosslink density and toughening effect of rubber modifiers, thereby testifying to their dissolution in the epoxy continuous phase.

The possible combination of rigid and soft particles could be a compromise to simultaneously improve both the tensile properties and the fracture toughness, which cannot be achieved by the single-phase particles independently.

Author Contributions: The study concept was devised by T.G.-K., A.A. and V.Š.; methodology, validation, and formal analysis were carried out by A.A., S.T. and T.G.-K.; the investigation, resources, and data curation were performed by L.S., T.G.-K., J.S., A.S., K.S. and A.Z.; writing—original draft preparation was performed by T.G.-K., A.A. and S.T.; supervision was performed by A.A.; project administration was performed by A.A. and V.Š. All authors have read and agreed to the published version of the manuscript.

Funding: This research was funded by M-Era.Net project MERF "Matrix for carbon reinforced epoxy laminates with reduced flammability" grant No. 1.1.1.5/ERANET/20/04 from the Latvian State Education Development Agency and M-Era.Net project "EPIC—European Partnership for Improved Composites" funded by grant No. TH06020001. A.S., K.S. and A.Z. are grateful to funding received from the European Union Horizon 2020 Framework program H2020-WIDESPREAD-01-2016-2017-TeamingPhase2 under grant agreement No. 739508, project CAMART2.

Institutional Review Board Statement: Not applicable.

Informed Consent Statement: Not applicable.

Data Availability Statement: Not applicable.

Conflicts of Interest: The authors declare no conflict of interest.

Appendix A

This Appendix presents the results of a three-dimensional finite element analysis of the grooved and flat TDCB specimens to investigate the influence of the geometrical parameters of the grooves on the stress intensity factor at the crack tip. The geometry of the TDCB sample that was used in this work was proposed in [16], and it is presented in Figure A1a. Grooves of different depths and shapes were analyzed by changing the angle γ of the grooves (45 and 90 degrees were used for simulations) and the internal radius R of the grooves, as shown in Figure A1b.

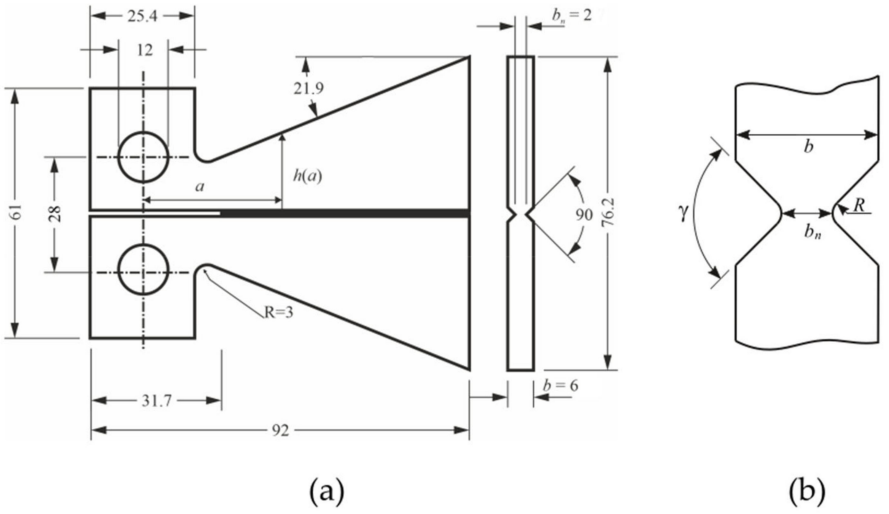

Figure A1. The geometry of the TDCB specimen with dimensions in millimeters (**a**) and a detailed view of the grooved section of the specimen (**b**).

The influence of the depth of the grooves on the SIF can be estimated using simple energy considerations and the known relation between the stress intensity factor and the

energy release rate. Assuming, that energy that is stored in the loaded arms of flat and grooved TDCB specimen is the same, the SIF of the grooved specimen can be written as

$$K_g = K_{ng}\left(\frac{b}{b_n}\right)^{0.5}, \tag{A1}$$

where K_{ng} is the SIF for a flat specimen defined in Equation (1). However, this simple analysis does not take into account the stress concentration at the bottom of the grooves. Freed and Craft [31] suggested an alternative form of Equation (A1):

$$K_g = K_{ng}\left(\frac{b}{b_n}\right)^{n}, \tag{A2}$$

where the value of exponent n is in the range $0.5 - 1$ and should be estimated through numerical analysis or by fitting the experimental data. The value $n = 1$ corresponds to the limiting case of a flat specimen with groves angle $\gamma = 180°$.

Lemmens et al. [32] used a 3D finite element simulation of grooved specimens and obtained the value of the exponent n in Equation (A2) to be equal 0.51 and 0.6 for the center and edge of the crack front, respectively. Gómez et al. [33] used a more complex model with a curved crack front and concluded that the best fit n value is close to 0.5. However, both of these works used grooves with an angle equal to 45° and no influence of the groove's sharpness was investigated.

In this work, finite element code ABAQUS was used to calculate the distribution of a stress intensity factor along the front of the initial pre-crack using the standard procedure that is available in ABAQUS. The finite element mesh of the grooved sample near the crack tip is shown in Figure A2a. Quadratic 15-node wedge elements were used for the whole model, except for the zone around the crack tip, where 20-node brick elements were generated in a circular manner with one-side-collapsed quarter point elements for the inner circle, as shown in Figure A2b. The calculations with different mesh densities showed that 15 elements through the specimen's width gave sufficient accuracy in the middle section of the crack, except for the small zones near the crack edges.

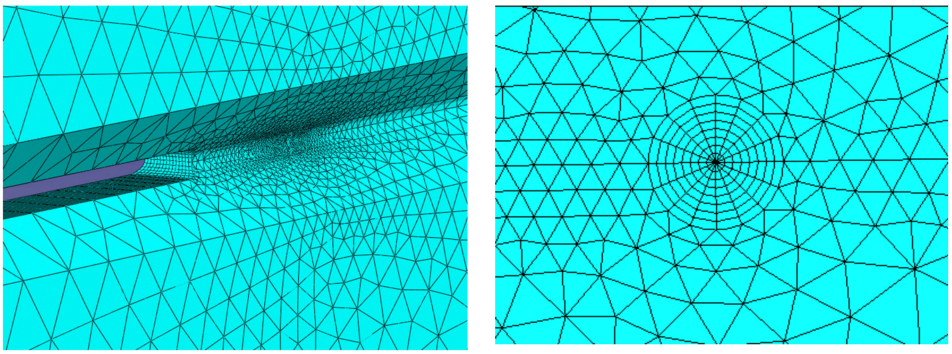

(**a**) (**b**)

Figure A2. Finite element mesh of a specimen with grooves (**a**) and arrangement of elements along the crack front for the calculation of stress intensity factors (**b**).

Several finite element models with a width of the specimen b that is equal to 6, 12 and 24 mm and different grooves geometries were analyzed. The SIF distribution along the crack front for a specimen with a width that is equal to 6 mm is presented in Figure A3, where the results are normalized with respect to the 2D plane strain solution in Equation (1). The results show that the SIF values gradually increase as the reduced width of the grooved specimen decreases. The side grooves also influence the SIF distribution along the crack front, making the SIF higher near the surface of the specimen, which is contrary to the flat specimen ($b/b_n = 1$), where the SIF is slightly higher at the center point of the crack front.

Figure A3a presents the results of the calculations for the specimens with different grooves angles, 45 and 90 degrees, respectively. The results show that the SIF is slightly higher for the grooves of 90°, which can be explained by the fact that more material is removed from the specimen in this case, thereby resulting in a higher compliance of the arms of a specimen under the same load. The influence of the sharpness of the grooves on the distribution of the SIF along the crack front is presented in Figure A3b, where the grooves with inner radii of 0.5, 0.25 and 0.15 mm were used for the calculations. As could be expected, the smaller that the inner radius of the grooves was, then the higher the SIF near the surface of the specimen was, however, at the same time, in the middle section of the specimen, the SIF is lower for the sharp grooves, resulting in almost the same average SIF for all three radii of the grooves.

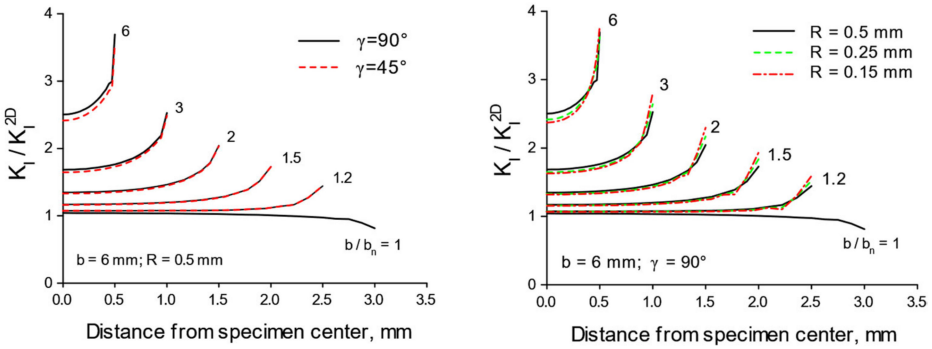

Figure A3. Stress intensity factor distribution along the crack front for grooves of different depths and two angles (**a**) and different radii at the tip of the groove (**b**). Numerical results are normalized by a two-dimensional solution.

The average values of the SIF along the crack front for different geometries of the grooves were approximated by a power function, and the results for the TDCB specimens with the width b that was equal to 6 mm and groove's angle that was equal to 45° and 90° are presented in Figure A4.

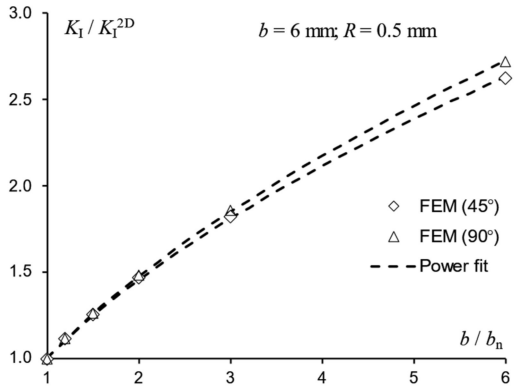

Figure A4. Approximation of the numerical data for the normalized average stress intensity factor by a power function.

The best fit values of the exponent n are listed in Table A1 for different geometries of the TDCB specimen and grooves.

Table A1. Exponent n value determined by fitting of simulations data for different grooves angles and specimen widths.

Grooves Angle γ	Specimen Width b, mm		
	6	**12**	**24**
45°	0.54	0.55	0.59
90°	0.56	0.59	0.65

References

1. Aniskevich, A.; Glaskova-Kuzmina, T. Effect of moisture on elastic and viscoelastic properties of fibre reinforced plastics: Retrospective and current trends. In *Creep and Fatigue in Polymer Matrix Composites*, 2nd ed.; Guedes, R.M., Ed.; Woodhead Publishing: Amsterdam, The Netherlands, 2019; pp. 83–120. [CrossRef]
2. Nunes, S.G.; Saseendran, S.; Joffe, R.; Amico, S.C.; Fernberg, P.; Varna, J. On Temperature-Related Shift Factors and Master Curves in Viscoelastic Constitutive Models for Thermoset Polymers. *Mech. Compos. Mater.* **2020**, *56*, 573–590. [CrossRef]
3. Giannakopoulos, G.; Masania, K.; Taylor, A.C. Toughening of epoxy using core-shell particles. *J. Mater. Sci.* **2011**, *46*, 327–338. [CrossRef]
4. Day, R.J.; Lovell, P.A.; Wazzan, A.A. Thermal and mechanical characterization of epoxy resins toughened using preformed particles. *Polym. Int.* **2001**, *50*, 849–857. [CrossRef]
5. Qian, J.Y.; Pearson, R.A.; Dimonie, V.L.; El-Aasser, M.S. Synthesis and application of core–shell particles as toughening agents for epoxies. *J. Appl. Polym. Sci.* **1995**, *58*, 439–448. [CrossRef]
6. Shen, J.; Zhang, Y.; Qiu, J.; Kuang, J. Core-shell particles with an acrylate polyurethane core as tougheners for epoxy resins. *J. Mater. Sci.* **2004**, *39*, 6383–6384. [CrossRef]
7. Quan, D.; Ivankovic, A. Effect of core-shell rubber (CSR) nano-particles on mechanical properties and fracture toughness of an epoxy polymer. *Polymer* **2015**, *66*, 16–28. [CrossRef]
8. Tang, L.C.; Zhang, H.; Sprenger, S.; Ye, L.; Zhang, Z. Fracture mechanisms of epoxy-based ternary composites filled with rigid-soft particles. *Compos. Sci. Technol.* **2012**, *72*, 558–565. [CrossRef]
9. Dadfar, M.R.; Ghadami, F. Effect of rubber modification on fracture toughness properties of glass reinforced hot cured epoxy composites. *Mater. Des.* **2013**, *47*, 16–20. [CrossRef]
10. Material Datasheet for CHS-Epoxy 582 by Spolchemie (Czech Republic). Available online: https://www.spolchemie.cz/en/product.chs-epoxy-582/?msclkid=77435be2bb3011ec852121a4067dc4ca (accessed on 11 August 2022).
11. Material Datasheet for Telalit 0420 by Spolchemie (Czech Republic). Available online: https://www.spolchemie.cz/en/product.telalit-0420/?msclkid=2065552fbb3111ec82d92b19f5b9d09c (accessed on 11 August 2022).
12. Material Datasheet for ACE MX-125, ACE MX-156, and ACE MX-960 by Kaneka (Belgium). Available online: https://www.kaneka.be/sites/default/files/uploads/brochures/MX/Kaneka-leaflet-Kane-Ace-Product-properties.pdf?msclkid=a2acc2d9bb3311ecb184043310b58907 (accessed on 11 August 2022).
13. Material Datasheet for Carbon Fabric by Havel Composites (Czech Republic). Available online: https://havel-composites.com/cs/produkty/uhlikova-tkanina-kc-160g-m2-3k-platno-s-120-cm-3568-4896 (accessed on 20 September 2022).
14. *ISO 527-1*; Plastics—Determination of Tensile Properties-Part 1: General Principles. ISO: Geneva, Switzerland, 2012.
15. *ISO 527-2*; Plastics—Determination of Tensile Properties-Part 2: Test Conditions for Moulding and Extrusion Plastics. ISO: Geneva, Switzerland, 2012.
16. Beres, W.; Ashok, K.K.; Thambraj, R. A tapered double-cantilever-beam specimen designed for constant-K testing at elevated temperatures. *J. Test. Eval.* **1997**, *25*, 536–542. [CrossRef]
17. *ASTM Standard D 5528-01*; Standard Test Method for Mode I Interlaminar Fracture Toughness of Unidirectional Fiber-Reinforced Polymer Matrix Composites. ASTM International: West Conshohocken, PA, USA, 2004.
18. Boon, Y.D.; Joshi, S.C. A review of methods for improving interlaminar interfaces and fracture toughness of laminated composites. *Mater. Today Commun.* **2022**, *22*, 100830. [CrossRef]
19. ImageJ Software. Available online: https://imagej.nih.gov/ij/index.html (accessed on 11 August 2022).
20. *ASTM Standard E 1545-01*; Standard Test Method for Assignment of the Glass Transition Temperature by Thermomechanical Analysis. ASTM International: West Conshohocken, PA, USA, 2002.
21. Van Velthem, P.; Gabriel, S.; Pardoen, T.; Bailly, C.; Ballout, W. Synergy between phenoxy and CSR tougheners on the fracture toughness of highly cross-linked epoxy-based composites. *Polymers* **2021**, *13*, 2477. [CrossRef] [PubMed]
22. Glaskova-Kuzmina, T.; Zotti, A.; Borriello, A.; Zarrelli, M.; Aniskevich, A. Basalt fibre composite with carbon nanomodified epoxy matrix under hydrothermal ageing. *Polymers* **2021**, *13*, 532. [CrossRef] [PubMed]
23. Glaskova-Kuzmina, T.; Aniskevich, A.; Papanicolaou, G.; Portan, D.; Zotti, A.; Borriello, A.; Zarrelli, M. Hydrothermal aging of an epoxy resin filled with carbon nanofillers. *Polymers* **2020**, *12*, 1153. [CrossRef] [PubMed]
24. Forental', G.A.; Sapozhnikov, S.B. Numerical-experimental estimation of the mechanical properties of an epoxy nanocomposite. *Mech. Compos. Mater.* **2011**, *47*, 521–528. [CrossRef]

25. Lagzdins, A.; Zilaucs, A.; Beverte, I.; Andersons, J.; Cabulis, U. A refined strut model for describing the elastic properties of highly porous cellular polymers reinforced with short fibers. *Mech. Compos. Mater.* **2017**, *53*, 321–334. [CrossRef]
26. Hansen, T.C. Influence of aggregate and voids on modulus of elasticity of concrete, cement mortar, and cement paste. *Int. Concr. Abstr. Portal* **1965**, *62*, 193–216. [CrossRef]
27. Yoshitake, I.; Rajabipour, F.; Mimura, Y.; Scanlon, A. A prediction method of tensile Young's modulus of concrete at early age. *Adv. Civ. Eng.* **2012**, *2012*, 391214. [CrossRef]
28. Becu, L.; Maazouz, A.; Sautereau, H.; Gerard, J.F. Fracture behavior of epoxy polymers modified with core-shell rubber particles. *J. Appl. Polym. Sci.* **1997**, *65*, 2419–2431. [CrossRef]
29. Quan, D.; Mischo, C.; Binsfeld, L.; Ivankovic, A.; Murphy, N. Fracture behaviour of carbon fibre/epoxy composites interleaved by MWCNT- and graphene nanoplatelet-doped thermoplastic veils. *Compos. Struct.* **2020**, *235*, 111767. [CrossRef]
30. Ning, H.; Li, J.; Hu, N.; Yan, C.; Liu, Y.; Wu, L.; Liu, F.; Zhang, J. Interlaminar mechanical properties of carbon fiber reinforced plastic laminates modified with graphene oxide interleaf. *Carbon* **2015**, *91*, 224–233. [CrossRef]
31. Freed, C.; Krafft, J. Effect of side grooving on measurements of plane-strain fracture toughness. *J. Mater.* **1966**, *1*, 770–790.
32. Lemmens, R.J.; Dai, Q.; Meng, D.D. Side-groove influenced parameters for determining fracture toughness of self-healing composites using a tapered double cantilever beam specimen. *Theor. Appl. Fract. Mech.* **2014**, *74*, 23–29. [CrossRef]
33. Garoz Gómez, D.; Gilabert, F.A.; Tsangouri, E.; Van Hemelrijck, D.; Hillewaere, X.K.D.; Du Prez, F.E.; Van Paepegem, W. In-depth numerical analysis of the TDCB specimen for characterization of self-healing polymers. *Int. J. Solids Struct.* **2015**, *64–65*, 145–154. [CrossRef]